

Viscoelastic Immersed Boundary Methods for Zero Reynolds Number Flow

Wanda Strychalski^{1,*}, Robert D. Guy¹

¹ *Department of Mathematics, University of California, Davis CA 95616, U.S.A.*

Abstract. The immersed boundary method has been extensively used to simulate the motion of elastic structures immersed in a viscous fluid. For some applications, such as modeling biological materials, capturing internal boundary viscosity is important. We present numerical methods for simulating Kelvin-Voigt and standard linear viscoelastic structures immersed in zero Reynolds number flow. We find that the explicit time immersed boundary update is unconditionally unstable above a critical boundary to fluid viscosity ratio for a Kelvin-Voigt material. We also show there is a severe time step restriction when simulating a standard linear boundary with a small relaxation time scale using the same explicit update. A stable implicit method is presented to overcome these computation challenges.

AMS subject classifications: 65M06,65M12,74F10,76D07,76M20

1 Background

Many challenging biological problems involve dynamic elastic structures immersed in an incompressible viscous flow. The immersed boundary method provides a way to simulate such problems. It was originally developed to simulate blood flow in the heart [23], but has been used for many biofluid applications with many different length and time scales. Some of these applications include platelet aggregation in blood clotting [10], insect flight [20], cellular biomechanics [28], cochlear dynamics [3], and many others. In each of these problems the solid structures were modeled as elastic objects.

Many biological materials are not adequately described as simply elastic materials, because they exhibit both viscous and elastic behavior [11, 26, 32]. For example, the cytoskeleton is a network of actin filaments, microtubules, and intermediate filaments that give animal cells their shape and ability to move [1]. On short time scales (seconds), the cytoskeleton behaves like an elastic solid, but on longer time scales (minutes) it acts like a viscoelastic fluid due to polymerization and depolymerization of actin filaments

*Corresponding author. *Email addresses:* wanda@math.ucdavis.edu (W. Strychalski), guy@math.ucdavis.edu (R. D. Guy)

[5, 18]. The cell reorganizes the cytoskeleton during motility, cell division, and mechanical interaction with its environment. The cytoskeleton has been modeled as a viscous fluid [33], viscoelastic fluid [9], viscoelastic solid [25], and elastic solid [30] depending on the context and the time scale of the cellular behavior. Elastic cytoskeletal models based on the immersed boundary formulation have been developed [4], and we are particularly interested in building upon our previous work on modeling the cytoskeleton [28]. A natural extension of these models would be to include different viscoelastic constitutive laws.

Elastic structures immersed in a viscoelastic fluid have been recently simulated [7, 29]. Viscoelasticity in structures has also been incorporated into the immersed boundary method in several ways [4, 12, 13, 16]. The cytoskeleton was modeled as a dynamic elastic network in [4], i.e. a network of elastic springs that form and break according to prescribed rules. It was shown in [4] that the material in this model behaved as a viscoelastic fluid, but it is not straightforward to extract the effective rheological properties from the local properties of the network. In [16], the authors simulate a two dimensional structure with finite mass immersed in a viscous fluid. The massive structure's motion is governed by a momentum equation that contains an internal friction proportional to the fluid velocity. A viscoelastic shell is modeled by a two dimensional elastic structure that encloses fluid in [13]. The viscous properties of the structure are inherited from the background fluid. Viscoelastic tether points where the immersed boundary force density is a function of the velocity and velocity history at boundary points were simulated in [12]. Each of these approaches included a structure viscosity in a different way. However, it is not clear how these approaches generalize to include different viscoelastic constitutive laws. A general study of viscoelastic immersed boundaries has not been done.

In this paper we investigate numerical methods to simulate a viscoelastic, massless, immersed boundary in zero Reynolds number flow. In Section 2, we present the fluid and viscoelastic constitutive equations. We consider two viscoelastic constitutive laws: the Kelvin-Voigt and standard linear models. The explicit immersed boundary algorithm is described in Section 3 with modifications for a viscoelastic boundary. Computational results for the explicit method are presented in Section 4. For the Kelvin-Voigt model, we show the explicit scheme is unconditionally unstable when the ratio of boundary to fluid viscosity is above a critical threshold. We also show the standard linear model has a severe time step restriction when the stress relaxation time scale is short. In this case, the constitutive law resembles that of the Kelvin-Voigt model. The explicit method for the Kelvin-Voigt model is analyzed in Section 5. In Section 6, we present a stable semi-implicit method to overcome the instability observed in the explicit Kelvin-Voigt method. We conclude with computational experiments and a convergence study of the semi-implicit method.

2 Mathematical Formulation

Our system consists of a boundary under tension immersed in a fluid. The fluid obeys Stokes equations,

$$\mu\Delta\vec{u}-\nabla p+\vec{f} = 0 \quad (2.1)$$

$$\nabla\cdot\vec{u} = 0, \quad (2.2)$$

where \vec{u} is the fluid velocity, μ is the fluid viscosity, p is pressure, and \vec{f} is the force density from the viscoelastic boundary transmitted to the fluid. Fluid quantities are represented by a fixed, Eulerian coordinate system. Lower case letters are used to distinguish fluid variables from variables associated with the boundary, which are indicated by capital letters.

The immersed boundary is denoted by $\Gamma=\vec{X}(s,t)$, where s parameterizes the curve and t represents time. A moving Lagrangian coordinate system is used to track the evolution of the boundary. It satisfies a no-slip boundary condition by moving with the fluid velocity,

$$\frac{d\vec{X}}{dt}=\vec{U}(s,t). \quad (2.3)$$

Tension or stress on the immersed boundary is denoted by $\sigma(t)$ and has both elastic and viscous components. The exact form of $\sigma(t)$ is described in the following subsections. The force density due to boundary tension can be computed by

$$F=\frac{\partial}{\partial s}(\sigma(t)\vec{\tau}), \quad (2.4)$$

where the tangent vector is

$$\vec{\tau}=\vec{X}_s/|\vec{X}_s|. \quad (2.5)$$

Following the immersed boundary formulation [23], the external force density \vec{f} from membrane tension is spread onto the fluid grid as follows,

$$\vec{f}(\vec{x},t)=\mathcal{S}(\vec{f})=\int_{\Gamma}\vec{F}(s,t)\delta(\vec{x}-\vec{X}(s,t))ds. \quad (2.6)$$

Similarly, interpolation from the fluid grid to the membrane grid is

$$\vec{U}(s,t)=\mathcal{S}^*(\vec{u})=\int_{\Omega}\vec{u}(\vec{x},t)\delta(\vec{x}-\vec{X}(s,t))d\vec{x}, \quad (2.7)$$

where Ω is the fluid domain.

In this manuscript, we consider the cases when the immersed boundary is modeled either as a Kelvin-Voigt viscoelastic solid or with the standard linear model. For a Kelvin-Voigt material, viscoelastic elements are represented by a spring and dashpot in parallel

(Fig. 1(a)). We chose this model because it is the simplest viscoelastic solid model. The constitutive law for a Kelvin-Voigt viscoelastic solid is

$$\sigma(t) = k\varepsilon(t) + \eta \frac{d\varepsilon(t)}{dt}, \quad (2.8)$$

where k is the spring constant, η is internal boundary viscosity, and ε strain. If a constant stress σ_0 is applied to a Kelvin-Voigt material, the resulting deformation exponentially approaches σ_0/k , the deformation of a purely elastic material. This behavior is known as “creep”. The relaxation time scale is η/k . For a constant strain, stress is constant, i.e. there is no stress relaxation. This is the same behavior as a purely elastic material.

The standard linear model is equivalent to a viscous and an elastic element in series parallel to an elastic element (Fig. 1(b)). This is the simplest model that exhibits both creep and stress relaxation. The constitutive law for a standard linear viscoelastic solid is

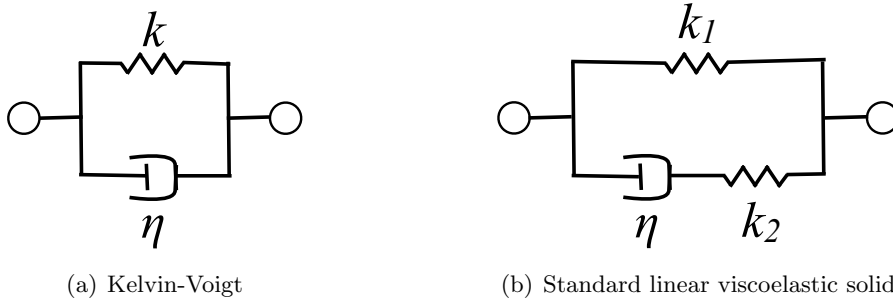


Figure 1: Diagrams of viscoelastic elements.

$$\frac{\eta}{k_2} \frac{d\sigma}{dt} + \sigma = \eta \frac{k_1 + k_2}{k_2} \frac{d\varepsilon}{dt} + k_1 \varepsilon, \quad (2.9)$$

where η is the viscosity of the material, and k_1 and k_2 are spring constants. If we take $\lambda = \eta/k_2$, $k = k_1$, and $k_2 \gg k_1$, the above equation becomes,

$$\lambda \frac{d\sigma}{dt} + \sigma = \eta \frac{d\varepsilon}{dt} + k\varepsilon, \quad (2.10)$$

where λ is called the stress relaxation time. If a constant strain ε_0 is loaded onto a standard linear material, stress exponentially approaches $k\varepsilon_0$ with timescale λ . The standard linear model also has a creep relaxation timescale η/k as in the Kelvin-Voigt model.

We take strain to be

$$\varepsilon = |\vec{X}_s|. \quad (2.11)$$

If the boundary were purely elastic, this would result in the constitutive law

$$\sigma = k|\vec{X}_s|. \quad (2.12)$$

When discretized, the boundary can be thought of as a collection of connected elastic springs with zero resting length and spring constant k . Similarly, the discretized viscoelastic boundary can be interpreted as connected viscoelastic elements (Fig. 1). From equations (2.3) and (2.11), the time derivative of strain is

$$\frac{d\varepsilon(t)}{dt} = \frac{d}{dt} \left(|\vec{X}_s| \right) = \frac{\vec{X}_s}{|\vec{X}_s|} \cdot \frac{d\vec{X}_s}{dt} = \frac{\vec{X}_s}{|\vec{X}_s|} \cdot \vec{U}_s = \vec{\tau} \cdot \vec{U}_s. \quad (2.13)$$

In our implementation of both constitutive laws, we use the above equation. For example, (2.8) becomes

$$\sigma(t) = k|\vec{X}_s| + \eta\vec{\tau} \cdot \vec{U}_s. \quad (2.14)$$

3 Numerical Formulation

Fluid quantities such as velocity and pressure are located on a fixed, staggered Eulerian grid (Fig. 2). The grid has size $N \times M$ with spacing Δx in the horizontal direction and

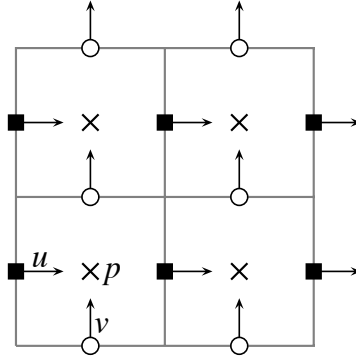


Figure 2: Staggered grid for fluid variables. The horizontal velocity component u is stored at filled squares. The vertical velocity component v is stored at circles. Pressure is stored at the center of the computational cell, denoted by crosses.

Δy in the vertical direction. Periodic boundary conditions are used on the fluid domain. The discretized boundary is located on a moving Lagrangian grid parameterized by s and contains N_b points with an initial uniform mesh spacing Δs .

Communication between grids is handled by the immersed boundary method [23]. The delta function in the spreading and interpolation operators (Eqs. (2.6) and (2.7)) is discretized in one dimension as follows,

$$\delta(x) \approx \delta_{\Delta x}(x) = \begin{cases} \frac{1}{4\Delta x} \left(1 + \cos\left(\frac{\pi x}{2\Delta x}\right) \right), & \text{if } |x| < 2\Delta x \\ 0, & \text{otherwise} \end{cases} \quad (3.1)$$

where Δx is the spatial step size. In two dimensions, we have $\delta(\vec{x}) \approx \delta_{\Delta x}(x)\delta_{\Delta y}(y)$. The discretization of the spreading operator Eq. (2.6) is

$$\vec{f}_{i,j}^{n+1} = \Delta s \sum_{\ell=1}^{N_b} \vec{F}_{\ell}^{n+1} \delta_{\Delta x}(x_i - X_{\ell}^n) \delta_{\Delta y}(y_j - Y_{\ell}^n), \quad (3.2)$$

where superscript indicates a term's location in time, i.e. $t^n = n\Delta t$. The discrete interpolation operator Eq. (2.7) is

$$\vec{U}_{\ell}^{n+1} = \Delta x \Delta y \sum_{ij} \vec{u}_{i,j}^{n+1} \delta_{\Delta x}(x_i - X_{\ell}^n) \delta_{\Delta y}(y_j - Y_{\ell}^n). \quad (3.3)$$

For the analysis provided later, it is important to note the spatial locations of boundary variables. The discretized variables \vec{F} and \vec{U} are located at boundary nodes \vec{X}_{ℓ} , while σ , $\vec{\tau}$, and \vec{U}_s are located at midpoints $\vec{X}_{\ell\pm 1/2}$ because we use centered differences to approximate spatial derivatives (Fig. 3). For example,

$$(D_{+1/2}\vec{X})_{\ell+1/2} = \frac{\vec{X}_{\ell+1} - \vec{X}_{\ell}}{\Delta s}, \quad (3.4)$$

and

$$(D_{-1/2}\sigma)_{\ell} = \frac{\sigma_{\ell+1/2} - \sigma_{\ell-1/2}}{\Delta s}. \quad (3.5)$$

Note that $D_{\ell-1/2}D_{\ell+1/2}$ is the standard 3-point Laplacian, and $D_{+1/2}^* = -D_{-1/2}$. For the remainder of the manuscript, A^* indicates the adjoint of the operator A .

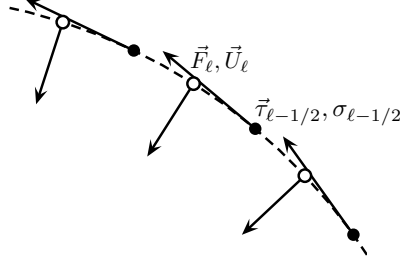


Figure 3: Spatial location of discretized boundary variables. The boundary is indicated by a dashed line. Solid circles indicate variables stored at the $\ell_{\pm 1/2}$ location. White circles are the boundary positions are variables at the ℓ th point.

The standard explicit algorithm for the immersed boundary method involves fractional time stepping. We attempt this method first because a fully implicit temporal update would involve solving a large nonlinear system of equations. One time step of the explicit method proceeds as follows:

1. Compute boundary forces using the viscoelastic constitutive law and current boundary configuration. The time discretization of the Kelvin-Voigt model (2.14) is

$$\sigma^{n+1}(t) = k\varepsilon^n + \eta \frac{d\varepsilon^n}{dt}. \quad (3.6)$$

Substituting equations (2.11) and (2.13) into the above equation yields,

$$\sigma^{n+1}(t) = k|\vec{X}_s|^n + \eta \vec{r} \cdot \vec{U}_s^n. \quad (3.7)$$

Discretizing the previous equation in space gives us,

$$\sigma^{n+1}(t) = k|D_{+1/2}\vec{X}^n| + \eta \frac{D_{+1/2}\vec{X}^n}{|D_{+1/2}\vec{X}^n|} \cdot D_{+1/2}\mathcal{S}\vec{u}^n. \quad (3.8)$$

The force density then is

$$\vec{F} = D_{-1/2} \left(\sigma^{n+1} \frac{D_{+1/2}\vec{X}^n}{|D_{+1/2}\vec{X}^n|} \right). \quad (3.9)$$

2. Spread the forces to the discretized fluid grid using (3.2).
3. Solve the fluid equations (2.1) and (2.2). Specifically, we take the divergence of (2.1) to obtain the equation $\Delta p = \nabla \cdot \vec{f}$. Spatial derivatives are approximated by centered differences. The discrete Fourier transform is used to solve the resulting linear system. Once the pressure is obtained, (2.1) is solved for each velocity component.
4. Interpolate the fluid velocity to discretized boundary points using (3.3).
5. Update the boundary points with (2.3),

$$\frac{\vec{X}^{n+1} - \vec{X}^n}{\Delta t} = \vec{U}^{n+1}. \quad (3.10)$$

4 Computational Results

We use a standard test from immersed boundary literature to benchmark our viscoelastic immersed boundary method. The viscoelastic boundary is initialized as an ellipse immersed in a viscous fluid. Internal pressure is generated because the unstressed boundary length is zero. The equilibrium boundary configuration is a circle of the same volume as the initial ellipse due to incompressibility of the fluid [17, 19, 27, 31]. Unless otherwise noted, the computational parameters are as follows. The computational domain is the unit box with 32×32 grid points. The spatial step size of the boundary is $\Delta s = \Delta x/2$, which results in 100 discrete boundary points. The fluid viscosity μ is 1 P. The semimajor of the ellipse axis is initially 0.4 cm, and the semiminor axis is 0.15625 cm. The equilibrium boundary configuration is a circle of radius 0.25 cm. To compare the dynamics in simulations across different parameter values, we compute the distance from the center of the ellipse at (0.5,0.5) to the right-most point on the boundary (Fig. 4).

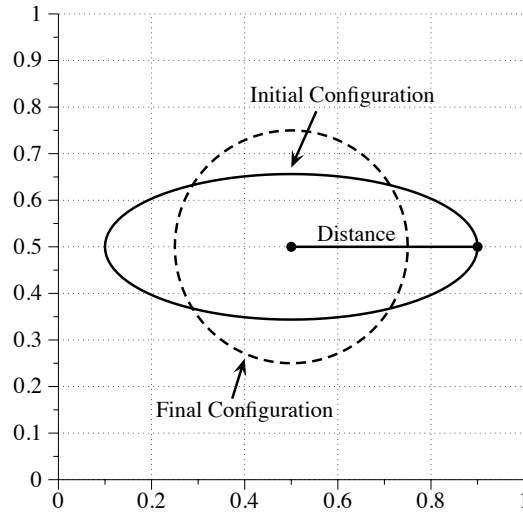


Figure 4: The boundary is initially an ellipse centered on the unit box. The equilibrium boundary position is a circle of radius 0.25. The distance from the center of mass to the right-most point is used to compare simulations with different parameters.

4.1 Explicit method for a Kelvin-Voigt boundary

For the test in this section, we follow the algorithm described in Section 3. Tension is computed using (2.14) discretized as described in the previous section. We use a spring constant $k = 10 \text{ g/s}^2$ and a time step $\Delta t = 0.001$. When there is no boundary viscosity, the boundary reaches a circular configuration at about $t = 0.5 \text{ s}$. When the boundary viscosity is increased to $\eta = 0.1 \text{ g s}^{-1}$, there is no noticeable change in the simulation output from the case of no boundary viscosity. The L^∞ norm of the difference in the distance measurements is 7.05×10^{-4} . The simulation is unstable when η is increased to 1 g s^{-1} . To determine whether a smaller time step improved the stability of the method, we systematically reduced the time step by an order of magnitude until $\Delta t = 10^{-12}$. In each case, boundary oscillations and unbounded growth were observed in the computation. This suggests there is a critical boundary viscosity above which the numerical method is unstable. We computed the maximum boundary viscosity η_c where the method was stable on two grid resolutions. Stability was determined by visualizing the boundary positions for oscillations. If no oscillations or unbounded growth were observed for at least 1000 time steps, the computation was deemed stable. The results are summarized in Table 4.1, accurate to two decimal places. Note that the Lagrangian spatial step size is refined with the Eulerian grid step size because we take $\Delta s = \Delta x/2$. The critical viscosity appears to approach a fixed value as $\Delta t \rightarrow 0$. This value also appears to depend on Δx because it is reduced by the same factor as the grid refinement. We will further analyze the stability of the explicit method in Section 5.

Δt	η_c	
	$\Delta x = 1/32$	$\Delta x = 1/64$
1×10^{-3}	0.48	0.23
1×10^{-4}	0.42	0.20
1×10^{-5}	0.39	0.19
1×10^{-6}	0.38	0.19

Table 1: Kelvin-Voigt Model: Largest boundary viscosity, called the critical viscosity η_c , for which the explicit method is stable for a given time step.

4.2 Explicit method for a standard linear boundary

We follow the same explicit temporal discretization scheme as described in Section 3. In the standard linear model, membrane tension is given by (2.10), which contains a time derivative of stress. We discretize $d\sigma/dt$ in (2.10) with backward Euler's method as follows,

$$\lambda \left(\frac{\sigma^{n+1} - \sigma^n}{\Delta t} \right) + \sigma^{n+1} = \eta \frac{d\varepsilon^n}{dt} + k\varepsilon^n, \quad (4.1)$$

with the initial condition $\sigma^0 = k\varepsilon$. The spatial discretization of other terms in (4.1) are handled in the same way as in the Kelvin-Voigt model (3.8). We computed the standard test problem for 10 s, varying the boundary viscosity η with other parameters fixed at the values $k=1 \text{ g/s}^2$, $\mu=1 \text{ P}$, $\Delta x = 1/32$, $\Delta t = 0.001$, $\lambda=1 \text{ s}$. The results are shown in Figure 5. Increasing the boundary viscosity decreases the time scale of the system.

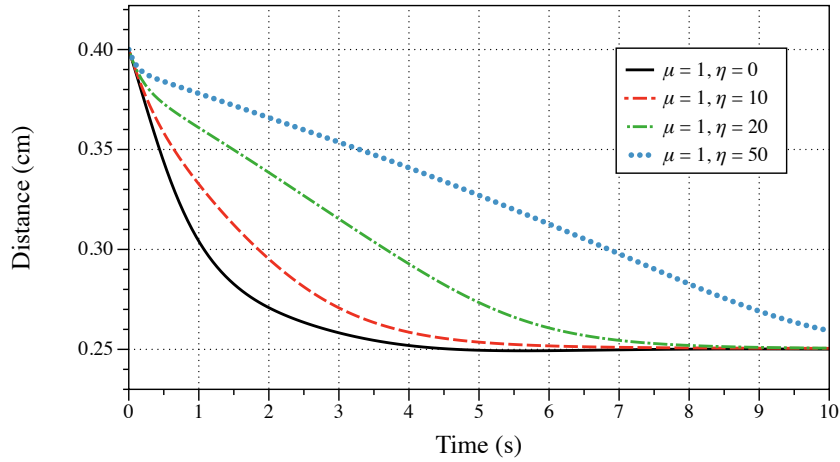


Figure 5: The distance from the boundary's center of mass to the rightmost point using the standard linear model for viscoelasticity. Increasing the boundary viscosity decreases the time scale.

When $\lambda=0$, the standard linear model reduces to the Kelvin-Voigt model. As λ tends

toward zero, we might expect a numerical instability to develop. We can rewrite (4.1) as

$$\sigma^{n+1} = \frac{\lambda}{\Delta t + \lambda} \sigma^n + \frac{k \Delta t}{\Delta t + \lambda} \varepsilon^n + \frac{\eta \Delta t}{\Delta t + \lambda} \frac{d\varepsilon^n}{dt}. \quad (4.2)$$

For small enough λ , the first term on the right hand side of the above equation is small. In this case, equation (4.2) resembles equation (3.6) (i.e. the Kelvin-Voigt model), but with different coefficients in front of each term. Because the explicit method was unstable above a critical viscosity η_c , we estimate the standard linear model will be stable if the coefficient in front of the strain time derivative is less than the critical viscosity observed in the Kelvin-Voigt simulations, i.e.

$$\frac{\eta \Delta t}{\Delta t + \lambda} < \eta_c \quad \text{or} \quad \Delta t < \frac{\lambda \eta_c}{\eta - \eta_c}. \quad (4.3)$$

The critical time step Δt_c is defined to be $\lambda \eta_c / (\eta - \eta_c)$. We simulated the standard problem for small λ in the regime where the Kelvin-Voigt model is unconditionally unstable with an explicit method. Parameters were chosen so that the time step would be restricted by λ rather than elastic stiffness ($\Delta x = 1/32$, $k = 1 \text{ g/s}^2$, $\mu = 1 \text{ P}$). Table 4.2 shows the maximum time step where the simulation was stable along with the corresponding critical time step. The time step data are accurate to three significant digits. The numerical results differ from the predicted critical time value by a factor of 10, but follow the same trend, that is $\Delta t = \mathcal{O}(\lambda)$. A possible reason for the discrepancy is that we assumed the first term on the right hand side in equation (4.2) was small in order to compare it to equation (3.6). However, this term is $\mathcal{O}(1)$ for the values of λ and Δt listed in Table 4.2. The computational time step must be small enough to resolve the physical time scale of the problem. The critical time step in the explicit method is set by the stress relaxation time λ . If the physical time scale of interest is much larger than the stress relaxation time scale, a semi-implicit method would avoid an unnecessarily small time step.

λ	Computed Δt	Δt_c
$\eta = 10$		
1×10^{-2}	5.35×10^{-3}	4.17×10^{-4}
1×10^{-3}	4.89×10^{-4}	4.17×10^{-5}
1×10^{-4}	4.76×10^{-5}	4.17×10^{-6}
$\eta = 100$		
1×10^{-2}	3.93×10^{-4}	4.02×10^{-5}
1×10^{-3}	3.90×10^{-5}	4.02×10^{-6}
1×10^{-4}	3.89×10^{-6}	4.02×10^{-7}

Table 2: Standard Linear Model time step restrictions for the case of small lambda, $\mu=1 \text{ P}$, and critical viscosity $\eta_c=0.4$, as computed in Table 4.1.

5 Analysis of the explicit method

In this section, we analyze the explicit method described in Section 3 to determine the cause of the instability observed when simulating a Kelvin-Voigt viscoelastic boundary. In this case, the the force density (2.4) is

$$\vec{F} = \frac{\partial}{\partial s} \left(k\vec{X}_s + \eta\vec{\tau} \cdot \vec{U}_s \vec{\tau} \right), \quad (5.1)$$

or alternatively,

$$\vec{F} = \frac{\partial}{\partial s} \left(k\vec{X}_s + \eta\vec{\tau} \cdot \frac{\partial}{\partial s} (\mathcal{S}^*(\vec{u})) \vec{\tau} \right). \quad (5.2)$$

We define the elastic force as $\mathcal{A}_f = -kD_{-1/2}D_{+1/2}$, where $D_{+1/2}$ and $D_{-1/2}$ are defined in (3.4) and (3.5). Then the discretized spread force density can be written as,

$$\vec{f} = \mathcal{S}\vec{F} = -\mathcal{S}\mathcal{A}_f\vec{X} + \eta\mathcal{S}D_{-1/2}(\vec{\tau} \cdot D_{+1/2}(\mathcal{S}^*\vec{u})\vec{\tau}). \quad (5.3)$$

Note that $\vec{\tau} \cdot D_{+1/2}(\mathcal{S}^*\vec{u})$ is a scalar, so that

$$\vec{f} = -\mathcal{S}\mathcal{A}_f\vec{X} + \eta\mathcal{S}D_{-1/2}\vec{\tau}(\vec{\tau} \cdot D_{+1/2}\mathcal{S}^*\vec{u}). \quad (5.4)$$

Because $D_{+1/2}^* = -D_{-1/2}$, and the above equation can be written as

$$\vec{f} = -\mathcal{S}\mathcal{A}_f\vec{X} - \eta\mathcal{S}D\vec{\tau}(\vec{\tau} \cdot D^*\mathcal{S}^*(\vec{u})), \quad (5.5)$$

where $D = D_{-1/2}$. Substituting the back into the fluid equation (2.1), the discretized system becomes

$$\begin{aligned} \mu L\vec{u}^{n+1} - \nabla p^{n+1} - \mathcal{S}\mathcal{A}_f\vec{X}^n - \eta\mathcal{S}D\vec{\tau}\vec{\tau} \cdot D^*\mathcal{S}^*\vec{u}^n &= 0 \\ \nabla \cdot \vec{u}^{n+1} &= 0 \\ \frac{\vec{X}^{n+1} - \vec{X}^n}{\Delta t} &= \mathcal{S}^*\vec{u}^{n+1}. \end{aligned} \quad (5.6)$$

We denote the boundary viscosity term by $\tilde{L} = -(\mathcal{S}D\vec{\tau})(\mathcal{S}D\vec{\tau})^*$. To analyze the above system of equations, we ignore incompressibility and pressure and focus on the solution for the fluid velocity during one time step,

$$\mu L\vec{u}^{n+1} = -\eta\tilde{L}\vec{u}^n + \mathcal{S}\mathcal{A}_f\vec{X}^n, \quad (5.7)$$

or

$$\vec{u}^{n+1} = -\frac{\eta}{\mu}L^{-1}\tilde{L}\vec{u}^n + (\mu L^{-1})\mathcal{S}\mathcal{A}_f\vec{X}^n. \quad (5.8)$$

The velocity grows in time if

$$\left\| \frac{\eta}{\mu}L^{-1}\tilde{L} \right\|_2 > 1. \quad (5.9)$$

The operator \tilde{L} looks like a Laplacian operator on a singularly concentrated set, and so one might expect that $\|L^{-1}\tilde{L}\|_2 = \mathcal{O}(1)$. However, the spreading operator \mathcal{S} scales like $\Delta s \Delta x^{-1} \Delta y^{-1} = \mathcal{O}(\Delta x^{-1})$, the interpolation operator $\mathcal{S}^* = \mathcal{O}(1)$, and so $\|L^{-1}\tilde{L}\|_2 = \mathcal{O}(\Delta x^{-1})$. We estimate that

$$\left\| \frac{\eta}{\mu} L^{-1} \tilde{L} \right\|_2 = \mathcal{O} \left(\frac{\eta}{\mu} \Delta x^{-1} \right). \quad (5.10)$$

The above estimate is consistent with data in Table 4.1, where the critical viscosity decreases as the grid was refined. The right hand side of (5.10) depends on the boundary configuration and grid spacing, but is independent of the time step. Therefore, there is a critical value of η/μ , above which the scheme is unstable for any time step. The instability is not seen in the standard linear model because stress has a relaxation time scale λ . The coefficient in front of the strain time derivative in (4.2) can be made small by reducing the time step. Stress does not instantaneously equilibrate as in the Kelvin-Voigt model unless λ is small.

6 Semi-implicit method

In order to simulate either a Kelvin-Voigt immersed boundary or standard linear model with small λ in zero Reynolds number flow, we propose a semi-implicit method similar to Newren et al. [22]. In the semi-implicit method, the spreading and interpolation operators are linearized by lagging them in time, i.e. they are computed by using boundary points from the previous time step t^n . All other unknowns are computed at the updated time step t^{n+1} . The discretized system is

$$\begin{aligned} (\mu L - \eta \mathcal{S} D \vec{\tau} \vec{\tau}^* D^* \mathcal{S}^*) \vec{u}^{n+1} - \nabla p^{n+1} - \mathcal{S} \mathcal{A}_f \vec{X}^{n+1} &= 0 & (6.1) \\ \nabla \cdot \vec{u}^{n+1} &= 0 \\ \frac{\vec{X}^{n+1} - \vec{X}^n}{\Delta t} &= \mathcal{S}^* \vec{u}^{n+1}. \end{aligned}$$

The system can be rewritten as

$$(\mu L + \eta \tilde{L} - \Delta t \mathcal{S} \mathcal{A}_f \mathcal{S}^*) \vec{u}^{n+1} - \nabla p^{n+1} = \mathcal{S} \mathcal{A}_f \vec{X}^n \quad (6.2)$$

$$\nabla \cdot \vec{u}^{n+1} = 0 \quad (6.3)$$

$$\frac{\vec{X}^{n+1} - \vec{X}^n}{\Delta t} = \mathcal{S}^* \vec{u}^{n+1}. \quad (6.4)$$

An advantage of this formulation is that the boundary unknowns are eliminated from the fluid equations. Equations (6.2) and (6.3) are solved simultaneously with a direct solve. However, the velocity is only uniquely determined up to an additive constant for Stokes flow with periodic boundary conditions [2]. The matrix is augmented so that it is uniquely solvable. The additional constraint is that the fluid variables \vec{u} and p have mean zero. After obtaining the fluid velocity, boundary points are updated according to (6.4).

6.1 Stability

We prove the semi-implicit method given by (6.2) - (6.4) is unconditionally stable by showing the energy of the discretized system is decreasing [22]. The relevant energy for our system has the form

$$E[\vec{X}] = \langle \mathcal{A}_f \vec{X}, \vec{X} \rangle_{\Gamma_d} = \|\vec{X}\|_{\mathcal{A}_f}^2. \quad (6.5)$$

Recall $\mathcal{A}_f = -kD_{-1/2}D_{+1/2}$. Because \mathcal{A}_f is a positive definite matrix, it defines an inner product. The discretization of the inner product on $L^2(\Gamma)$ is

$$\langle \vec{X}, \vec{Y} \rangle_{\Gamma_d} = \sum_{\ell} \vec{X}_{\ell} \cdot \vec{Y}_{\ell} \Delta s. \quad (6.6)$$

The operators \mathcal{S} and \mathcal{S}^* are adjoints, i.e.

$$\langle \mathcal{S} \vec{F}, \vec{w} \rangle_{\Omega_d} = \langle \vec{F}, \mathcal{S}^* \vec{w} \rangle_{\Gamma_d}. \quad (6.7)$$

The inner product $\langle \cdot, \cdot \rangle_{\Omega_d}$ is the discretized $L^2(\Omega)$ inner product:

$$\langle \vec{v}, \vec{w} \rangle_{\Omega_d} = \sum_{i,j} \vec{v}_{i,j} \cdot \vec{w}_{i,j} \Delta x \Delta y. \quad (6.8)$$

Taking the \mathcal{A} -norm squared of (6.4), we have

$$\|\vec{X}^{n+1} - \Delta t \mathcal{S}^* \vec{u}^{n+1}\|_{\mathcal{A}}^2 = \|\vec{X}^n\|_{\mathcal{A}}^2, \quad (6.9)$$

which is equivalent to

$$\|\vec{X}^{n+1}\|_{\mathcal{A}}^2 + \Delta t^2 \|\mathcal{S}^* \vec{u}^{n+1}\|_{\mathcal{A}}^2 - 2 \langle \vec{X}^{n+1}, \Delta t \mathcal{S}^* \vec{u}^{n+1} \rangle_{\mathcal{A}} = \|\vec{X}^n\|_{\mathcal{A}}^2. \quad (6.10)$$

Next we take the dot product of \vec{u}^{n+1} with (6.2), yielding

$$\langle \vec{u}^{n+1}, (\mu L + \eta \tilde{L}) \vec{u}^{n+1} \rangle_{\Omega_d} - \langle \vec{u}^{n+1}, \mathcal{S} \mathcal{A}_f \vec{X}^{n+1} \rangle_{\Omega_d} = 0, \quad (6.11)$$

because divergence-free velocity fields are orthogonal to gradient fields in our discretization, i.e. $\langle \vec{u}^{n+1}, \nabla p^{n+1} \rangle_{\Omega_d} = 0$. From the above equation, we have

$$\langle \vec{u}^{n+1}, (\mu L + \eta \tilde{L}) \vec{u}^{n+1} \rangle_{\Omega} = \langle \vec{u}^{n+1}, \mathcal{S} \mathcal{A}_f \vec{X}^{n+1} \rangle_{\Omega} = \langle \mathcal{S}^* \vec{u}^{n+1}, \mathcal{A}_f \vec{X}^{n+1} \rangle_{\Gamma} = \langle \mathcal{S}^* \vec{u}^{n+1}, \vec{X}^{n+1} \rangle_{\mathcal{A}}. \quad (6.12)$$

Combining (6.12) and (6.10) gives us

$$\|\vec{X}^{n+1}\|_{\mathcal{A}}^2 + \Delta t^2 \|\mathcal{S}^* \vec{u}^{n+1}\|_{\mathcal{A}}^2 - 2 \Delta t \langle \vec{u}^{n+1}, (\mu L + \eta \tilde{L}) \vec{u}^{n+1} \rangle_{\Omega} = \|\vec{X}^n\|_{\mathcal{A}}^2, \quad (6.13)$$

or equivalently,

$$E[\vec{X}^{n+1}] = E[\vec{X}^n] - \Delta t^2 \|\mathcal{S}^* \vec{u}^{n+1}\|_{\mathcal{A}}^2 + 2 \Delta t \langle \vec{u}^{n+1}, (\mu L + \eta \tilde{L}) \vec{u}^{n+1} \rangle_{\Omega_d}. \quad (6.14)$$

Examining the two terms on the right hand side, we see that $\|\mathcal{S}^* \vec{u}^{n+1}\|_{\mathcal{A}}^2$ is clearly positive. The term $\mu L + \eta \tilde{L}$ is negative definite because both the Laplacian and \tilde{L} operators are negative definite. Then we have

$$E[\vec{X}^{n+1}] < E[\vec{X}^n]. \quad (6.15)$$

Therefore, the potential energy is decreasing with each time step, and the scheme is unconditionally stable.

6.2 Computational results

In this section, we use the semi-implicit method to simulate the standard test described in Section 4. Because the explicit method was unstable for small η , we were unable to determine how increasing the boundary viscosity affected the dynamics for the Kelvin-Voigt model. The distance from the rightmost point on the ellipse to the center of mass for several different boundary values of η is shown in Figure 6. Other parameters were held fixed at $\Delta x=1/32$, $\Delta t=0.01$, $k=10 \text{ g/s}^2$, $\mu=1 \text{ P}$. Figure 6 shows that increasing the

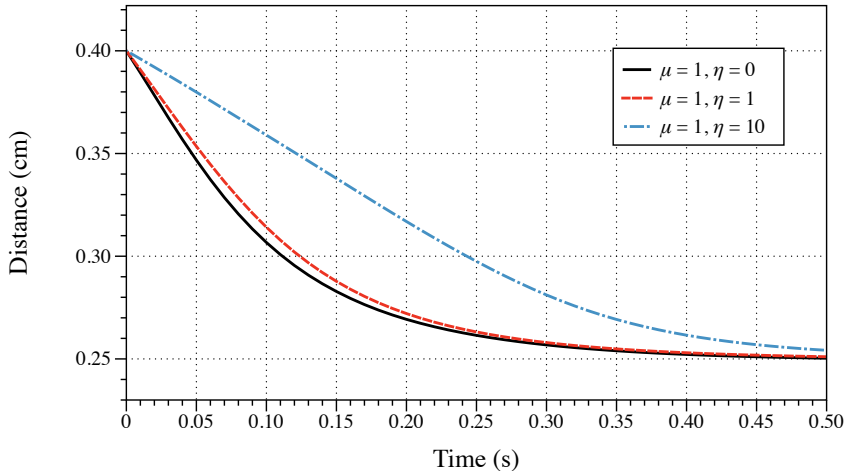


Figure 6: The distance from the boundary's center of mass to the rightmost point using the Kelvin-Voigt model for viscoelasticity. Increasing the boundary viscosity decreases the time scale.

boundary viscosity decreases the time scale of the system. There is only a small change between the no boundary viscosity and $\eta=1 \text{ g/s}$ case. The boundary viscosity must be high relative to the fluid viscosity to see a large change in the dynamics. The explicit method is always unstable in that regime, and an implicit method must be used.

Next we test the convergence of the semi-implicit method in the regime of large boundary viscosity. We simulated the standard test problem until 0.5 s with $k=10 \text{ g/s}^2$ and $\eta=10 \text{ g/s}$. The spatial Lagrangian and Eulerian grids as well as the time step were refined by a factor of 1.5. The Eulerian grid spacing was $\Delta x=\Delta y=1/N$, and the Lagrangian grid spacing was defined to be $\Delta s=\Delta x/2$. The time step Δt was chosen to be $\Delta t=1/(2N)$. The grid sizes used were $N=32, 48, 72$, and 108. The measure of error is the difference between the distance from the rightmost most of the ellipse to the center of mass of the boundary on successive grid refinements. The convergence data and power function fit are shown in Figure 7. Based on our test, the method converges with at least first order accuracy.

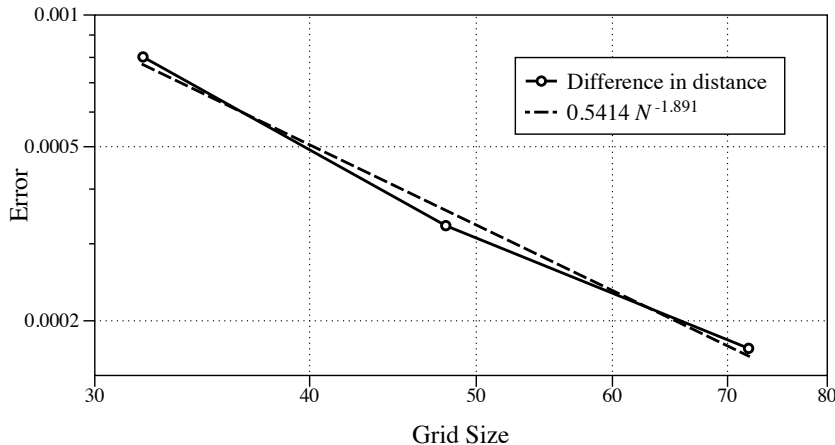


Figure 7: Convergence data for the semi-implicit method plotted on a logarithmic scale. Error is defined as the difference in distance from the rightmost boundary point to the boundary’s center of mass for successive grid refinements. The dashed line plot is the power function fit to the data.

7 Discussion

We have presented computational methods to simulate viscoelastic models of an immersed boundary in zero Reynolds number flow. When the boundary is purely elastic, tension is only a function of the current boundary configuration. In the viscoelastic case, tension also depends on the history of deformation. For the viscoelastic models that we considered, this dependence leads to spatial derivatives of velocity in the constitutive equations. This resulted in additional numerical stiffness that was observed when we simulated the viscoelastic models with the explicit temporal immersed boundary scheme. We discovered a critical viscosity ratio above which the Kelvin-Voigt model was always unstable. Additionally, we found a time step restriction for small stress time relaxation in the standard linear model. We presented a semi-implicit discretization for the Kelvin-Voigt model and proved its stability. The scheme could also be used with the standard linear model. Our implementation of the method was not designed for efficiency; we used a direct solve to invert the linear system. However, it may be possible to use efficient solvers designed for implicit immersed boundary equations [6, 14, 15, 21]. Alternatively in zero Reynolds number flow, boundary integral methods [24] or the method of regularized Stokeslets [8] are appropriate to simulate the systems described in this manuscript. When the boundary is purely elastic, the force density is calculated from the current boundary configuration. In the viscoelastic case, the force density is a function of velocity derivatives so that an integral equation must be solved to extract the boundary force density.

Viscous stresses typically lead to a time step restriction for an explicit method, and not unconditional numerical instability. In the Kelvin-Voigt model, the viscous forces are given by $(\mu L + \eta \tilde{L}) \vec{u}$, where \tilde{L} is a localized Laplacian that arises from boundary viscosity. In the explicit method for the Kelvin-Voigt model, part of the viscous forces are lagged in

time. If the lagged viscous boundary forces become too large relative to the viscous fluid forces, the explicit scheme becomes unconditionally unstable. In the Kelvin-Voigt model, the viscous stress is determined by the instantaneous strain rate, while in the standard linear model the viscous stress depends on time history of the strain rate. This difference is reflected in the discretized stress equations (3.6) and (4.2) for the Kelvin-Voigt model and standard linear model, respectively. In the explicit method for the standard linear model, the discrete time step can always be made small enough to avoid numerical instability.

In zero Reynolds number flow, there is no inertia and forces are instantaneously equilibrated. An explicit time scheme could be used with any boundary viscosity in the Kelvin-Voigt model. The coefficient in front of the force density term in the time-discretized momentum equation would be multiplied by a time step that could be made arbitrarily small. However, for a large boundary viscosity there may be a severe time step restriction in the explicit scheme. In this case, the implicit method may be needed.

Many biological structures exhibit viscoelastic properties, and it may be important to include viscous effects in models in order to describe the biological behavior. In our simple test problem, the effect of boundary viscosity seemed only to slow the relaxation of the boundary to equilibrium. For more complicated problems, including boundary viscosity may have significant effects on the dynamics.

Acknowledgments

This work was supported in part by the NIH Glue Grant ‘Cell Migration Consortium’ (NIGMS U54 GM64346) to Alex Mogilner as well as by NSF-DMS grant 0540779 and UCOP grant 09-LR-03-116724-GUYR to RG.

References

- [1] B. Alberts, A. Johnson, J. Lewis, M. Raff, K. Roberts, and P. Walter. *Molecular biology of the cell*. Garland Science, New York, 4th edition, 2002.
- [2] G.K. Batchelor. *An Introduction to Fluid Dynamics*. Cambridge University Press, Cambridge, 1967.
- [3] Richard P. Beyer, Jr. A computational model of the cochlea using the immersed boundary method. *J. Comput. Phys.*, 98:145–162, 1992.
- [4] D. C. Bottino. Modeling viscoelastic networks and cell deformation in the context of the immersed boundary method. *J. Comput. Phys.*, 147(1):86 – 113, 1998.
- [5] D. Bray. *Cell movements: from molecules to motility*. Garland Science, New York, 2nd edition, 2001.
- [6] H. D. Ceniceros, J. E. Fisher, and A. M. Roma. Efficient solutions to robust, semi-implicit discretizations of the immersed boundary method. *J. Comput. Phys.*, 228:7137–7158, 2009.
- [7] J.C. Crispell, R. Cortez, D.B. Khismatullin, and L.J. Fauci. Shape oscillations of a droplet in an oldroyd-b fluid. *Physica D: Nonlinear Phenomena*, In Press, 2011.
- [8] R. Cortez. The method of regularized stokeslets. *SIAM J. Sci. Comput.*, 23(4):1204–1225, 2001.

- [9] C. Dong, R. Skalak, K. L. Sung, G. W. Schmid-Schönbein, and S. Chien. Passive deformation analysis of human leukocytes. *J. Biomech. Eng.*, 110(1):27–36, 1988.
- [10] A. L. Fogelson. A mathematical model and numerical method for studying platelet adhesion and aggregation during blood clotting. *J. Comput. Phys.*, 56(1):111 – 134, 1984.
- [11] Y. C Fung. *Biomechanics: mechanical properties of living tissues*. Springer-Verlag, New York, 2nd edition, 1993.
- [12] D. Goldstein, R. Handler, and L. Sirovich. Modeling a no-slip flow boundary with an external force field. *J. Comput. Phys.*, 105(2):354 – 366, 1993.
- [13] B.E. Griffith and C.S. Peskin. On the order of accuracy of the immersed boundary method: Higher order convergence rates for sufficiently smooth problems. *J. Comput. Phys.*, 208(1):75–105, 2005.
- [14] R.D. Guy and B. Philip. A multigrid method for a model of the implicit immersed boundary equations. *Commun. Comput. Phys. in press*, 2011.
- [15] T. Y. Hou and Z. Shi. An efficient semi-implicit immersed boundary method for the navier-stokes equations. *J. Comput. Phys.*, 227:8968–8991, 2008.
- [16] W. X. Huang and H. J. Sung. An immersed boundary method for fluid-flexible structure interaction. *Comput. Method. Appl. M.*, 198(33-36):2650–2661, 2009.
- [17] R. J. LeVeque and Z. Li. Immersed interface methods for stokes flow with elastic boundaries or surface tension. *SIAM J. Sci. Comput.*, 18(3):709–735, 1997.
- [18] M. Mayer, M. Depken, J. S. Bois, F. Jülicher, and S. W. Grill. Anisotropies in cortical tension reveal the physical basis of polarizing cortical flows. *Nature*, 467(7315):617–21, 2010.
- [19] A. A. Mayo and C. S. Peskin. An implicit numerical method for fluid dynamics problems with immersed elastic boundaries. *Fluid Dynamics in Biology: Proc. AMS–IMS–SIAM Joint Summer Research Conf. on Biofluidynamics*, 141 of *Contemporary Mathematics*, AMS:261–277, 1993.
- [20] L. A. Miller and C. S. Peskin. When vortices stick: an aerodynamic transition in tiny insect flight. *J. Exp. Biol.*, 207(17):3073–3088, 2004.
- [21] Y. Mori and C. S. Peskin. Implicit second-order immersed boundary methods with boundary mass. *Comp. Method. Appl. M.*, 197(25-28):2049 – 2067, 2008. Immersed Boundary Method and Its Extensions.
- [22] E. P. Newren, A. L. Fogelson, R. D. Guy, and R. M. Kirby. Unconditionally stable discretizations of the immersed boundary equations. *J. Comput. Phys.*, 222(2):702 – 719, 2007.
- [23] C. S. Peskin. Numerical analysis of blood flow in the heart. *J. Comput. Phys.*, 25(3):220–252, 1977.
- [24] C. Pozrikidis. *Boundary integral and singularity methods for linearized viscous flow*, volume 7. Cambridge University Press, Cambridge, 1992.
- [25] G. W. Schmid-Schönbein, K. L. Sung, H. Tözeren, R. Skalak, and S. Chien. Passive mechanical properties of human leukocytes. *Biophys. J.*, 36(1):243–56, 1981.
- [26] D. Stamenović. Rheological behavior of mammalian cells. *Cell. Mol. Life. Sci.*, 65(22):3592–605, 2008.
- [27] J. M. Stockie and B. R. Wetton. Analysis of stiffness in the immersed boundary method and implications for time-stepping schemes. *J. Comput. Phys.*, 154:41–64, 1998.
- [28] W. Strychalski and R.D. Guy. A computational model of bleb formation. *submitted*, 2011.
- [29] J. Teran, L. Fauci, and M. Shelley. Viscoelastic Fluid Response Can Increase the Speed and Efficiency of a Free Swimmer. *Phys. Rev. Lett.*, 104(3):038101, 2010.
- [30] D. P. Theret, M. J. Levesque, M. Sato, R. M. Nerem, and L. T. Wheeler. The application of a homogeneous half-space model in the analysis of endothelial cell micropipette measurements.

- J. Biomech. Eng.*, 110(3):190–9, 1988.
- [31] C. Tu and C. S. Peskin. Stability and instability in the computation of flows with moving immersed boundaries: a comparison of three methods. *SIAM J. Sci. Stat. Comput.*, 13:1361–1376, 1992.
- [32] F. Wottawah, S. Schinkinger, B. Lincoln, R. Ananthakrishnan, M. Romeyke, J. Guck, and J. Kas. Optical rheology of biological cells. *Phys. Rev. Lett.*, 94(9), 2005.
- [33] A. Yeung and E. Evans. Cortical shell-liquid core model for passive flow of liquid-like spherical cells into micropipets. *Biophys. J.*, 56(1):139–49, 1989.